PHYSICAL REVIEW E **97**, 012902 (2018)

Effect of particle stiffness on contact dynamics and rheology in a dense granular flow

S. Bharathraj and V. Kumaran
Department of Chemical Engineering, Indian Institute of Science, Bangalore 560 012, India

(Received 1 November 2017; published 9 January 2018)

Dense granular flows have been well described by the Bagnold rheology, even when the particles are in the multibody contact regime and the coordination number is greater than 1. This is surprising, because the Bagnold law should be applicable only in the instantaneous collision regime, where the time between collisions is much larger than the period of a collision. Here, the effect of particle stiffness on rheology is examined. It is found that there is a rheological threshold between a particle stiffness of 10^4–10^5 for the linear contact model and 10^5–10^6 for the Hertzian contact model above which Bagnold rheology (stress proportional to square of the strain rate) is valid and below which there is a power-law rheology, where all components of the stress and the granular temperature are proportional to a power of the strain rate that is less then 2. The system is in the multibody contact regime at the rheological threshold. However, the contact energy per particle is less than the kinetic energy per particle above the rheological threshold, and it becomes larger than the kinetic energy per particle below the rheological threshold. The distribution functions for the interparticle forces and contact energies are also analyzed. The distribution functions are invariant with height, but they do depend on the contact model. The contact energy distribution functions are well fitted by Gamma distributions. There is a transition in the shape of the distribution function as the particle stiffness is decreased from 10^7 to 10^6 for the linear model and 10^8 to 10^7 for the Hertzian model, when the contact number exceeds 1. Thus, the transition in the distribution function correlates to the contact regime threshold from the binary to multibody contact regime, and is clearly different from the rheological threshold. An order-disorder transition has recently been reported in dense granular flows. The Bagnold rheology applies for both the ordered and disordered states, even though the rheological constants differ by orders of magnitude. The effect of particle stiffness on the order-disorder transition is examined here. It is found that when the particle stiffness is above the rheological threshold, there is an order-disorder transition as the base roughness is increased. The order-disorder transition disappears after the crossover to the soft-particle regime when the particle stiffness is decreased below the rheological threshold, indicating that the transition is a hard-particle phenomenon.

DOI: 10.1103/PhysRevE.97.012902

I. INTRODUCTION

An intriguing feature of the dense granular flows, repeatedly reported in simulations of simple shear flows or flows down an inclined plane, is the validity of the Bagnold relationship [1–3] between the stress and the rate of deformation [4–7]. All components of the stress are found to be proportional to the square of the strain rate. The Bagnold relationship is a dimensional requirement if the only time scale is the inverse of the strain rate, and there is no "material" time scale associated with the interparticle contacts. This, in turn, implies that the period of a contact is small compared to the inverse of the strain rate, and is often interpreted as implying that the system is in the rapid flow regime where the contacts between particles are through instantaneous collisions. However, the Bagnold relationship is found to be valid even when the system is in the multibody contact regime, and the coordination number (number of particles in simultaneous contact with a test particle) is greater than 1. Further, it is now established that there is very little change in the rheology as the strain rate is changed and the system transitions from a binary contact regime to the multibody contact regime [8,9]. There have been some explanations for this unusual behavior, such as the dominance of one contact even in a multibody contact regime in the force transmission to a particle [5]. However, this puzzling phenomenon has still not been well understood.

Here, simulations using the LAMMPS simulation package are carried out for the flow of spherical particles down an inclined plane. The flow down an inclined plane is a apt model flow for studying rheology, since the volume fraction in the core of the flow is a constant to within the simulation resolution [4–6]. This is counterintuitive; it would naively be expected that the volume fraction would increase with depth due to the greater overburden. However, simulations have repeatedly shown that the volume fraction is independent of height in the bulk. Here, we examine whether the volume fraction continues to be a constant as the particle stiffness is reduced to very small values.

The particle stiffness is usually expressed in dimensionless form, $[k/(mg/d)]$, for the linear contact model (where the stiffness k has dimensions of force per unit length), and $[k/(mg/d^{1/2})]$ for the Hertzian contact model [where the stiffness k has dimensions of (force/length$^{3/2}$)]. Here, m is the mass of a particle, d is the particle diameter, and g is the acceleration due to gravity. Real particles such as sand grains and glass beads with size 100 μm to 1 mm have dimensionless stiffness in the range 10^8–10^{11}. Simulations are typically carried out with much softer particles with stiffness in the range 10^4–10^6 in order to reduce the computation time, since the contact time scales as $\sqrt{m/k}$ for the linear contact model, and the simulation time step has to be much smaller than the contact time.

The effect of particle stiffness on the rheology and the contact time was analyzed by Silbert *et al.* [10] for the flow down an inclined plane. In the simulations of Silbert *et al.* [10], the velocity profile was fitted to a combination of a linear and a Bagnold profile, and the ratio of the relative measures of the linear and Bagnold profiles was used to identify the parameter regimes under which the Bagnold rheology was valid. The deviation from the Bagnold profile was found to be less than 10% when the nondimensional particle stiffness is greater than about 10^4 for the linear contact model, and greater than about 10^5 for the Hertzian contact model. The authors reported, for the first time, a correlation between the contact lifetime and the rheology. The probability distribution of the time of contact is strongly peaked at the collision time, and has an exponentially decaying tail for large contact times. Based on a criterion for identifying the lifetime of long-lived contacts τ_l, the authors showed that the deviation from Bagnold rheology is strongly correlated to $\dot{\gamma}\tau_l$, the product of the strain rate and the characteristic contact time of long-lived contacts.

We examine the validity of the Bagnold rheology in relation to the coordination number, the granular temperature (kinetic energy per particle), the contact force, and contact energy magnitudes. One open question is why Bagnold rheology appears to be valid even in the multibody contact regime, though the theoretical justification is limited to the binary contact regime. Clearly, Bagnold rheology has a validity wider than its derivation, and it is of interest to examine other parameters which correlate with the particle stiffness regime for the validity of Bagnold rheology. Another important issue is the magnitude of the kinetic energy per particle, contact forces and contact energies in the flowing state, and whether these depend on the particle stiffness.

The contact forces and force distributions have been measured for static piles, and there has been a lot of work on the distribution of forces at the bottom of a static heap [11] or under quasistatic deformation [12,13]. Theoretical studies [14–16] using diverse approaches have predicted exponential distributions for the magnitude of the interparticle contact forces in a static granular pile. Velocity distributions for the particles in the flowing state have been extensively studied for vibrated [17–19] and sheared [20–25] granular materials. Kinetic theory methods have also been used to derive constitutive relations [26–30] and the effect of correlations on the constitutive relations has been examined [31–33]. Kinetic theories have been used for dense granular flows down an inclined plane [7,24,25]. Attempts have been made to bridge the gap between the flowing and static states by including a finite period of contact in the context of kinetic theories [34], and critical scalings have been extracted for the rheology as a function of volume fraction near jamming [35,36]. However, the evolution of the contact energies and forces in the flowing state has not been examined so far. It is of interest to relate the force and energy distributions to the strain rate and the fluctuating velocities, in order to smoothly progress from the flowing to the static state as the angle of inclination is decreased for the flow down an inclined plane. Here, we study the distribution of contact forces and energies in the flowing state, and examine whether these depend on the particle contact model and the binary or multibody contact regime. It is also of interest to examine whether there is a shift in the distribution functions when the system progresses from the Bagnold to non-Bagnold rheology as the particle stiffness is decreased.

A recently reported phenomenon is the transition from a disordered to an ordered state as the base roughness is decreased in the dense granular flow down an inclined plane [37–39]. Different types of base roughness have been studied, such as ordered and disordered frozen-particle bases where the base consists of a layer of static particles in random or hexagonally ordered arrangements, as well as sinusoidal bases with modulation in the flow and spanwise directions [40]. The base roughness is defined as the ratio of the frozen and moving particle diameters for frozen-particle bases, and the ratio of the sinusoidal amplitude and the moving particle diameter for sinusoidal bases. A discontinuous transition from a disordered to an ordered state is observed when the base roughness is decreased by as little as 1%. The ordered and disordered states have very different properties. There are distinct layers of particles parallel to the base sliding over each other in the ordered state, with in-plane hexagonal ordering of particles within the layers. There is no ordering in the random state when the base particle roughness exceeds the critical value. The volume fraction in the ordered state is higher than that in the random state, and could even exceed the random close packing volume fraction of 0.64. The Bagnold relation is satisfied in both the ordered and random states, but the Bagnold coefficients (ratio of stress and square of strain rate) are very different. For equal stress, the strain rate in the ordered state is one order of magnitude higher than that in the random state.

The order-disorder transition in the granular flow down an inclined plane appears to be similar to the crystallization transition in rigid hard-particle systems, where there is a transition from a random state to face centered cubic ordering at a volume fraction of 0.49 for spherical particles in three dimensions [41–45]. While the reasons for ordering in an inclined plane flow, which is the base roughness, are different from those for hard spheres at equilibrium, which is the balance between configurational and communal entropy [46], there are aspects of both transitions which are poorly understood; this is despite decades of research on the ordering in hard-particle systems. Here, we study a more basic question, whether the order-disorder transition in the dense granular flow down an inclined plane is in fact a hard-particle phenomenon, by examining the transition for different values of the particle stiffness.

II. SYSTEM AND SIMULATION METHODOLOGY

The simulations are carried out using LAMMPS, a molecular dynamics package, for the flow of monodisperse spheres over an inclined plane. The linear and Hertzian spring-dashpot models [47] are used for the interparticle interactions; these are not described in detail here, because they have been discussed extensively elsewhere [4,39]. The models consist of a resistive particle force perpendicular to the surface of contact which depends on the normal overlap δ_n (the difference between the center-to-center distance of the particles and the sum of particle radii) and a normal damping force which

TABLE I. The average normal overlap $\bar{\delta}_n$ as a function of the particle stiffness for the linear and Hertzian contact models.

Linear model		Hertzian model		
k_n	$\bar{\delta}_n$	k_n	$\bar{\delta}_n$	Symbol
5×10^2	6.33×10^{-2}	2×10^3	5.58×10^{-2}	○
10^3	3.50×10^{-2}	10^4	2.25×10^{-2}	△
10^4	4.75×10^{-3}	10^5	5.94×10^{-3}	▽
10^5	5.47×10^{-4}	10^6	1.42×10^{-3}	◁
10^6	6.26×10^{-5}	10^7	3.81×10^{-4}	▷
10^8	1.07×10^{-6}	10^8	9.15×10^{-4}	◇

depends on the relative velocity perpendicular to the surface of contact. The resistive force is proportional to δ_n for the linear model, and $\delta_n^{3/2}$ for the Hertzian model. In the direction parallel to the surface of contact, the tangential force is first computed as the sum of a spring force which depends on the tangential displacement, and a damping force which depends on the tangential velocity. There are also two types of contacts, sticking and sliding contacts, depending on the relative magnitudes of the tangential and normal forces. If the computed tangential force is less than the friction coefficient times the normal force, the sticking contact model is used, where the tangential force is computed from the tangential displacement and velocity. If the computed tangential force is greater than the friction coefficient times the normal force, the tangential force is set equal to the product of the friction coefficient and the normal force. In the simulations, the normal spring constant k_n is varied over 6–8 orders of magnitude, while the ratio of the tangential and normal spring coefficients (k_t/k_n) is set equal to (2/7). The normal damping coefficient γ_n for the linear model is selected such that the normal coefficient of restitution $e_n = \exp(-\gamma_n t_{col}/2)$ is 0.6, where γ_n is the damping constant and the collision time $t_{col} = \pi(2k_n/m - \gamma_n^2/4)^{-1/2}$. This requires that $(\gamma_n^2/k_n) = 0.20$. The ratio of the tangential and normal damping coefficients, (γ_t/γ_n), is set equal to 1/2. The friction coefficient is 0.4 in all the simulations. The reasons for selecting these ratios were discussed in detail in [4].

When the particle stiffness is decreased, the overlap increases. The linear and Hertzian approximations for the resistive forces are valid only when the overlap is small, and these cannot be used when the overlap becomes comparable to the particle diameter. Therefore, care is taken to ensure that the maximum overlap is less than about 6% of the particle diameter for the lowest values of the particle stiffness used here. The average overlap in the simulations $\bar{\delta}_n$, averaged over the entire flow, is shown as a function of the particle stiffness in Table I.

The length of the simulation box is 40 particle diameters, the width is 20 particle diameters, and 64 000 moving particles are simulated, resulting in a height of about 70 particle diameters. The angle of inclination is 22° in all our simulations, since we are interested in the effect of particle stiffness on rheology. Periodic boundary conditions are employed in the flow and spanwise directions with a solid surface below and a free surface at the top. The base is either a bumpy base with a disordered or ordered configuration of particles glued to it, or a smooth wall with a sinusoidal modulation. The properties in the bulk are independent of the base configuration. Most of the results presented here are for a hexagonally ordered frozen-particle base with a base particle diameter 1.5 times the moving particle diameter for the disordered flow. The base particle diameter is decreased below 1.34 times the moving particle diameter to attain an ordered state. The preparation of these different base topographies and their influence on the rheology have been elaborated in [40].

The simulations are advanced in time steps of 0.02 times $\sqrt{m/k_n}$ for the linear contact model since the period of a collision is comparable to $\sqrt{m/k_n}$, where m is the particle mass and k_n is the particle stiffness. The same numerical value is also used for the Hertzian contact model, though the collision time is greater for the Hertzian contact model. The simulation box is initially prepared with the base horizontal, and particles are poured in at random locations. The box is then tilted to an angle of 22° to initiate the flow. The time required for reaching steady state is about 800 dimensionless time units, where the time is scaled by $\sqrt{d/g}$, where d is the particle diameter and g is the gravitational acceleration. After this, the properties are measured over 1000 configurations spanning 8 time units. The mean value is the average over the entire simulation run of 8 time units, while the standard deviations are calculated from the average values for four subsequences of 2 dimensionless time units each. The standard deviation in the volume fraction is much smaller than the symbol size, so these are not shown in Figs. 1(a) and 1(c). The standard deviations for the coordination number are shown in Figs. 1(b) and 1(d), those for the strain rate are shown in Fig. 2, the force magnitude

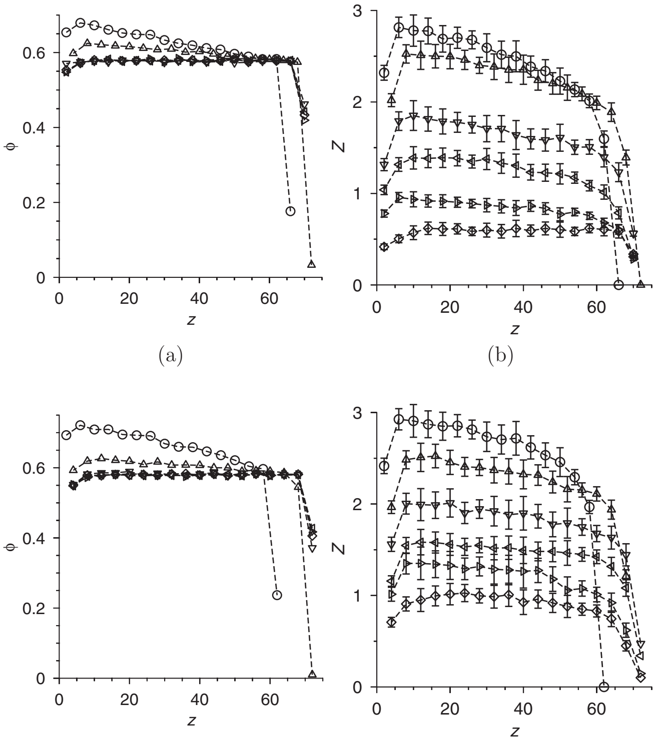

(a) (b)

(c) (d)

FIG. 1. The variation in the volume fraction ϕ [(a) and (c)] and the coordination number Z [(b) and (d)] with height z for different values of the particle stiffness k_n for the linear contact model [(a) and (b)] and the Hertzian contact model [(c) and (d)]. The parameters for the different symbols are provided in Table I.

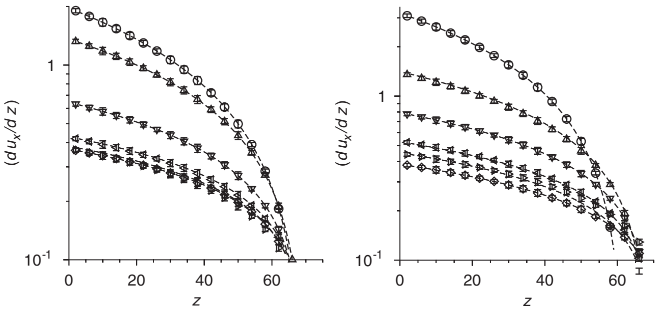

(a) (b)

FIG. 2. The variation of the strain rate with height for different values of the particle stiffness k_n for the linear contact model (a) and the Hertzian contact model (b). The parameters for the different symbols are provided in Table I.

in Fig. 6, and the kinetic and potential energies in Fig. 8. The standard deviations in the coordination number and the strain rate are about 5%. There are larger standard deviations of about 8%–10% in the force magnitude, and the kinetic and contact energies per particle, but these appear relatively small because the variations in these quantities span many orders of magnitude.

In the analysis, the x axis is along the flow direction parallel to the base, the z axis is perpendicular to the base, and the y axis is in the spanwise direction perpendicular to the flow and parallel to the base. The results are all expressed in nondimensional form, where the particle diameter d is used to scale length, the particle mass m is used to nondimensionalize mass, and time is nondimensionalized by $\sqrt{d/g}$, where g is the acceleration due to gravity.

III. RHEOLOGY

The density profiles for different values of the particle stiffness for the linear and Hertzian models are shown in Figs. 1(a) and 1(c), respectively. The symbols used for the different particle stiffnesses are given in Table I. For particle stiffness in the range 10^8–10^4 for the linear model and in the range 10^8–10^5 for the Hertzian model, the volume fraction is independent of height in the bulk. There are regions of height about 5 particle diameters at the top and at the base where the volume fraction deviates from the constant value due to boundary effects. This constant volume fraction in the bulk is now well understood for hard-particle systems where the Bagnold rheology is valid. When the particle stiffness decreases to 10^3 and below for the linear contact model and 10^4 and below for the Hertzian contact model, there is a distinct increase in the volume fraction with increased depth due to the greater overburden. In fact, at the lowest value of 5×10^2 for the linear model and 2×10^3 for the Hertzian model, the volume fraction at the base is higher than the random close packing volume fraction of 64%. This is not surprising, because the random close packing limit of 64% is applicable only for hard-particle systems, and the overlap between very soft particles could increase the volume fraction beyond this limit. It is also noteworthy that due to the increase in the volume fraction, the height of the flowing layer has decreased from about 70 particle diameters to about 65 particle diameters when the particle stiffness is decreased to 5×10^2 for the linear model and 2×10^3 for the Hertzian model.

In contrast to the volume fraction, the average coordination number Z increases continuously as the particle stiffness is decreased, as shown in Figs. 1(b) and 1(d). The coordination number is less than 1, as assumed in the binary collision approximation, only for the highest stiffness of 10^7 and higher for the linear contact model, and 10^8 and higher for the Hertzian contact model. For all other values of the particle stiffness, the coordination number is 1 or larger. Interestingly, the coordination number increases with depth even for cases where the volume fraction is independent of depth, such as for $10^4 \leqslant k_n \leqslant 10^7$ for the linear model and $10^5 \leqslant k_n \leqslant 10^8$ for the Hertzian models. Thus, there is a range of values of the particle stiffness for which the coordination number increases with height, but the volume fraction is independent of height. In this range, the effect of the increased overburden is reflected in the increased coordination number even though there is no increase in the volume fraction.

The strain rate, shown in Fig. 2, is plotted on a log-linear graph, in order to accommodate the variation of over a decade in the strain rate with height. The salient feature of the strain rate profiles is that they are relatively invariant with particle stiffness when the stiffness is above a threshold, but there is a sharp increase in the strain rate when the stiffness decreases below this threshold. For the linear contact model, there is virtually no change in the strain rate when the particle stiffness decreases from 10^8 to 10^5, but there is an increase by a factor of 4 when the particle stiffness is decreased from 10^4 to 5×10^2. Similarly, for the Hertzian contact model, the strain rate shows very little variation with particle stiffness for $k_n \geqslant 10^6$, but there is a significant increase when the particle stiffness is decreased to 2×10^3. More importantly, there is a significant change in the scaling of the strain rate profiles with height. The dashed lines show fits of the form

$$(du_x/dz) \propto (h - z)^{\eta_\gamma}, \tag{1}$$

where η_γ is the power-law exponent. For particle stiffness 10^5 or greater for the linear model and about 10^6 or greater for the Hertzian model, the strain rate is proportional to $(h-z)^{1/2}$. This is expected from the Bagnold law where the stress is proportional to the square of the strain rate. However, when the particle stiffness is decreased, the exponent η_γ decreases. For the lowest particle stiffness of 5×10^2 for the linear model and 2×10^3 for the Hertzian model, the strain rate is proportional to $(h-z)$. This is expected for a Newtonian fluid where the stress is proportional to the strain rate at constant density. The variation of the exponent η_γ with particle stiffness is discussed a little later in Fig. 5.

The relationship between the stress and the strain rate is shown in Fig. 3. The normal stresses σ_{xx} and σ_{zz} are equal to within the resolution in the simulations, and so these are shown on the same graph. The ratio $(\sigma_{xz}/\sigma_{zz}) = \tan(\theta)$ from momentum balance, where θ is the angle of inclination. Since the angle θ is set to 22° in our simulations, the stress $\sigma_{xz} = 0.404\sigma_{zz}$, and so the shear stress has not been plotted separately. Though the normal stress in the spanwise direction, σ_{yy}, is smaller than σ_{xx} and σ_{zz} by about 8%, the scaling between σ_{yy} and (du_x/dz) is the same as that for the other normal stress components within simulation resolution, and so σ_{yy} is not plotted separately. It is evident from Fig. 3 that the stress-strain rate relationship is well described by a power-law

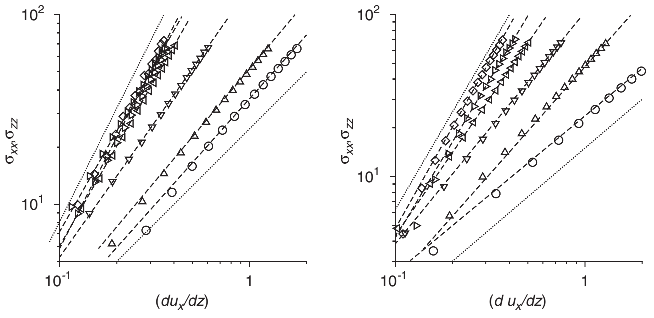

(a) (b)

FIG. 3. The variation of the normal stresses σ_{xx} and σ_{zz} as a function of (du_x/dz) for different values of the particle stiffness k_n for the linear contact model (a) and the Hertzian contact model (b). The dashed lines are power-law fits [Eq. (2)], the dotted line on the left shows $\sigma_{ij} \propto (du_x/dz)^2$, and the dotted line on the right shows $\sigma_{ij} \propto (du_x/dz)$. The parameters for the different symbols are provided in Table I, and the values of η_σ are shown as a function of the particle stiffness later in Fig. 5.

fit. For high values of the particle stiffness $k_n > 10^4$ for the linear contact model and $k_n > 10^5$ for the Hertzian contact model, all components of the stress are proportional to the square of the strain rate. When the particle stiffness decreases below 10^4 for the linear model and 10^5 for the Hertzian model, there is a significant departure from the Bagnold rheology, and the stress-strain rate relationship is linear for the lowest values of the particle stiffness. This appears to be similar to Newtonian rheology. However, it should be noted that for Newtonian fluids, the shear stress is proportional to the strain rate, and the pressure is determined from the incompressibility condition; in contrast, here, all components of the stress are proportional to the strain rate.

The scaled normal stress differences, $N_1 = (\sigma_{xx} - \sigma_{zz})/\sigma$ and $N_2 = (\sigma_{zz} - \sigma_{yy})/\sigma$, have also been calculated where $\sigma = (\sigma_{xx} + \sigma_{yy} + \sigma_{zz})/3$ is the negative of the pressure. The first normal stress difference is close to zero, while the second normal stress difference is about 10% in the simulations. The second normal stress difference is found to be nearly invariant with the particle stiffness.

The granular temperature, which is the kinetic energy per particle, is shown as a function of the strain rate on a log-log graph in Fig. 4. The dashed lines in this figure show power-law fits, and the dotted lines show slopes of 2 and 3/2 on a log-log graph. When the particle stiffness is high, Fig. 4 shows that the granular temperature is proportional to $(du_x/dz)^2$; this is expected for the hard-particle model where the collisions are considered to be instantaneous. As the particle stiffness decreases, the granular temperature is found to scale as $T^{3/2}$ for the lowest value of the particle stiffness considered here.

Power-law relations of the form

$$\sigma_{ij} \propto (du_x/dz)^{\eta_\sigma}, \tag{2}$$

$$\frac{3(\sigma_{zz} - \sigma_{yy})}{\sigma_{xx} + \sigma_{yy} + \sigma_{zz}} \propto (du_x/dz)^{\eta_{N2}}, \tag{3}$$

$$T \propto (du_x/dz)^{\eta_T} \tag{4}$$

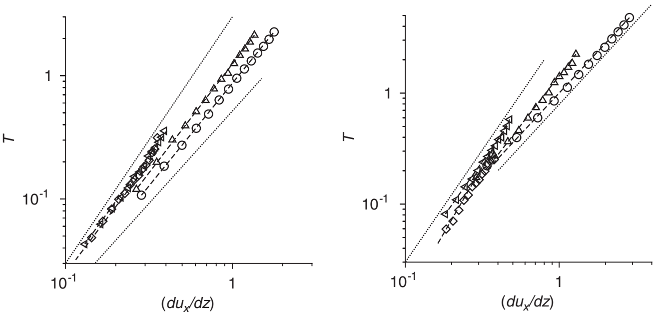

(a) (b)

FIG. 4. The variation of the kinetic energy per particle as a function of (du_x/dz) for different values of the particle stiffness k_n for the linear contact model (a) and the Hertzian contact model (b). The dashed lines show the fits to Eq. (4), the dotted line on the left shows $K \propto (du_x/dz)^2$, and the dotted line on the right shows $K \propto (du_x/dz)^{3/2}$. The parameters for the different symbols are provided in Table I, and the values of η_T are shown as a function of the particle stiffness later in Fig. 5.

have been fitted to the data in Figs. 3 and 4, where η_σ is the exponent for the stress fitted from the dashed lines in Fig. 3, η_{N2} is the exponent for the second normal stress difference, and η_T is the exponent for the granular temperature fitted from the lines in Fig. 4. These exponents are shown in Fig. 5, along with the coordination number and the exponent η_γ in Eq. (1), at different values of the particle stiffness. It is clear that there is a "rheological threshold" for the particle stiffness, which is in the interval 2×10^4 to 6×10^4 for the linear model and 2×10^5 to 6×10^5 for the Hertzian model. Above this threshold, the rheology is well described by Bagnold rheology, all components of the stress are proportional to the square of the strain rate, and the granular temperature is proportional to the square of the strain rate. The strain rate increases as the square root of the depth above the threshold. Below this threshold, there is a decrease in the exponent η_σ, to a minimum of 1 at the lowest particle stiffness considered here. The exponent for the granular temperature η_T decreases to about 1.5 for the smallest value of the particle stiffness considered here. The exponent

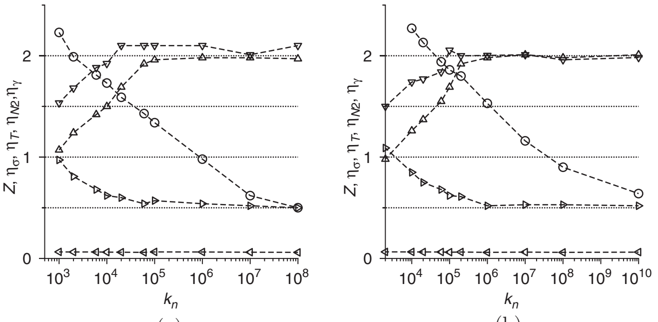

(a) (b)

FIG. 5. The height-averaged coordination number Z (○), the exponents η_σ in Eq. (2) (△), η_T in Eq. (4) (▽), η_{N2} in Eq. (3) (◁), and η_γ in Eq. (1) (▷), as a function of the particle stiffness k_n for the linear contact model (a) and Hertzian contact model (b). The dotted horizontal lines show the exponent values 0.5, 1.0, 1.5, and 2.0 for reference.

for the normal stress difference, η_{N2}, is found to be close to zero for both the linear and Hertzian contact model, and is invariant with particle stiffness, indicating that all components of the stress have the same power-law scaling with the strain rate.

Two other results are worth noting. First, the volume fraction profiles in Fig. 1 show that the volume fraction is independent of height when the particle stiffness is above the rheological threshold, while there is a variation in the volume fraction with height when the particle stiffness is below the rheological threshold. Second, the coordination number is about 1.5 or more at the rheological threshold for both the linear and Hertzian model, indicating that the system is not in the binary contact regime. Thus, Bagnold rheology appears to apply even when the system is in the multibody contact regime, and the invariance of the volume fraction with height is a consequence of the Bagnold rheology.

IV. CONTACT FORCE AND ENERGY

The time-averaged force on a particle due to interparticle interactions is equal to the gravitational force on the particle. However, the instantaneous magnitude of the net force on a particle could be higher than the time average of the force on a particle, and it provides a measure of the contact force fluctuations in the system, analogous to the kinetic energy fluctuations represented by the granular temperature. The contact regime is assessed using two force measures, the average magnitude of the instantaneous resultant force on a particle F_R, and the instantaneous sum of the magnitude of all the forces on a particle, F_M. If $\mathbf{F}_{ij}$ is the contact force between particles i and j, F_R and F_M are defined as

$$F_R = \frac{1}{N}\sum_{i=1}^{N}\left|\sum_{j=1}^{n_i}\mathbf{F}_{ij}\right|, \tag{5}$$

$$F_M = \frac{1}{N}\sum_{i=1}^{N}\sum_{j=1}^{n_i}|\mathbf{F}_{ij}|, \tag{6}$$

where N is the total number of particles considered for averaging, n_i is the number of particles instantaneously in contact with the particle i, and the summation is carried out over all neighboring particles. The measures F_R and F_M provide some insight into the contact regime in the flow. If the particle interactions are due to to instantaneous collisions in the hard-particle limit, the value of F_R and F_M will be comparable. In the dense multibody contact regime where the particle weight is balanced by multiple contact forces of approximately equal magnitude, the sum of the magnitude of all the forces F_M is expected to be much greater than the magnitude of the resultant F_R. The contact energy E_c is the integral of the force dotted with the differential displacement over the duration of a contact. For a contact between particles i and j, the contact energy is defined as a summation over the simulation time steps,

$$E_c = \sum_k \mathbf{F}_{ij}^k \cdot \Delta\mathbf{x}_{ij}^k, \tag{7}$$

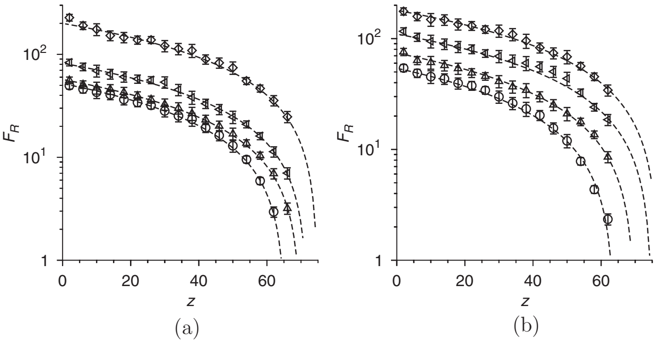

(a)

(b)

FIG. 6. The variation of the magnitude of the average resultant force on a particle F_R defined in Eq. (5) for the linear contact model (a) and the Hertzian contact model (b). The dashed lines show linear fits for the data. The parameter values for the different symbols are shown in Table I.

where $\mathbf{F}_{ij}^k$ is the force acting on particle i due to particle j in time step k, and $\Delta\mathbf{x}_{ij}^k$ is the differential relative displacement between the two particles in time step k. The summation is initiated when there is overlap, that is, the distance between two particles decreases below one particle diameter, and the contact energy is set to zero after breakage of the contact. The total contact energy over all contacts is divided by the number of contacts to determine the energy per contact, and by the total number of particles in the simulation to determine the contact energy per particle.

The average magnitude of the resultant force measure F_R is shown as a function of height for different values of the particle stiffness for the linear and Hertzian contact models in Fig. 6. The qualitative variation of the force measure F_M is similar to F_R. Figure 6 shows that F_R increases approximately linearly with depth, as expected from the linear increase of the overburden. To clearly discern the linear behavior in the log-linear graphs in Fig. 6, the linear fits are also shown by the dashed lines. The instantaneous force magnitude decreases faster for the lowest values of the particle stiffness, 5×10^2 for the linear model and 2×10^3 for the Hertzian model, due to the decrease in height that was also observed in Fig. 1. The instantaneous force magnitude increases by a factor of 4 when the particle stiffness increases by 5 orders of magnitude for the linear contact model, and when the particle stiffness increases by 7 orders of magnitude for the Hertzian contact model. Thus, the variation in the magnitude of the forces is relatively small compared to the variation in the magnitude of the particle stiffness for the linear and Hertzian models.

The height-averaged values of F_R and F_M are shown as a function of the particle stiffness in Fig. 7. The averaging is carried out only in the bulk of the flow, and particles in regions of height 5 particle diameters at the top and bottom are excluded, to avoid the effects of the ballistic layer of particles at the top and the particles in contact with the base at the bottom. The height-averaged values of F_R and F_M vary very little when the particle stiffness is varied over 5 orders of magnitude for both the linear and Hertzian contact models. The ratio (F_R/F_M), shown referenced to the right y axis on a linear scale in Fig. 7, does decrease monotonically as the particle stiffness is increased. However, this ratio varies in a

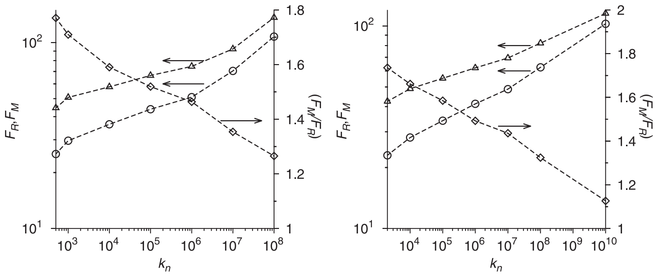

(a) (b)

FIG. 7. The height-averaged values of F_R defined in Eq. (5) (○) and F_M defined in Eq. (6) (△) referenced to the left y axis on a log scale, and the ratio (F_M/F_R) (◇) referenced to the right y axis on a linear scale, as a function of the particle stiffness for the linear contact model (a) and Hertzian contact model (b).

relatively narrow range from 1.8 and 1.2 as the particle stiffness is increased over five orders of magnitude for the linear model, and between 1.8 and 1.1 when the stiffness is increased over seven orders of magnitude for the Hertzian model. This appears to indicate that the resultant force on a particle is not due to a quasistatic balance between much larger forces exerted by neighboring particles even at the lowest value of the particle stiffness, but the contact forces are dominated by the largest force on a particle.

The contact energy per particle, E_c, exhibits characteristics that are very different from the force magnitude. The variation of the contact energy per particle E_c, along with the granular temperature T, is shown in Fig. 8. The granular temperature exhibits a power-law decrease with height in the bulk, and then a slower decrease near the top due to the ballistic layer of particles at the top. The contact energy per particle decreases much faster, because the frequency of collisions decreases to zero in the ballistic layer at the top. The contact energy is also found to be well fitted by power laws, as discussed below.

The contact energy per particle shows a large decrease as the particle stiffness is decreased, and there is a more modest decrease in the kinetic energy per particle. This is in contrast to the force magnitudes in Fig. 6, which increase as the particle stiffness is increased. There is a significant decrease in the contact energy per particle, by a factor greater than 10^4, when the particle stiffness is increased from 5×10^2 to 10^8 for the linear model. Similarly, for the Hertzian contact model, there is a decrease in the contact energy per particle by a factor of 10^4 when the particle stiffness increases from 2×10^3 to 10^8. In contrast, there is a modest decrease by a factor of about 10 in the kinetic energy per particle when the stiffness is increased from 5×10^2 to 10^8 for the linear model, and 2×10^3 to 10^8 for the Hertzian model. The height profiles of the kinetic and contact energies per particle are qualitatively similar, though the contact energy decreases faster with height than the kinetic energy near the top.

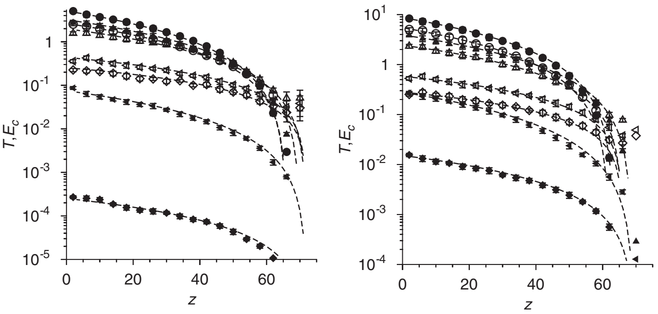

(a) (b)

FIG. 8. The variation of the kinetic energy per particle T (open symbols) and contact energy per particle E_c (filled symbols) as a function of height. The parameters for the different symbols are shown in Table I. The dashed lines show the power-law fits [Eq. (8)].

At low particle stiffness, for $k_n \leqslant 10^3$ for the linear model and $k_n \leqslant 10^4$ for the Hertzian model, the contact energy per particle is larger than the kinetic energy per particle. As the particle stiffness is increased beyond 10^4 for the linear contact model and 10^5 for the Hertzian contact model, the kinetic energy exceeds the contact energy per particle. For the highest particle stiffness considered here, T is greater than E_c by a factor greater than 10^3 for the linear contact model, and greater than 10 for the Hertzian contact model. Even though the contact energy per particle is numerically small compared to the kinetic energy per particle, a systematic variation is discernible in the height profiles of the contact energy per particle.

The dashed lines in Fig. 8 are power-law fits for the kinetic and contact energy per particle of the form

$$\begin{aligned} T &\propto (h-z)^{\eta_{Tz}}, \\ E_c &\propto (h-z)^{\eta_{Ez}}. \end{aligned} \tag{8}$$

Only the temperature variation in the bulk is used for the fits for the granular temperature, and the ballistic layer of height about 5 particle diameters at the top is excluded while calculating η_{Tz} in Eq. (8). From Fig. 8, it is evident that the exponents η_{Tz} and η_{Ez} are different from 1. This is in contrast to the fits for the force magnitudes in Fig. 6, which were found to increase linearly with depth. The power-law exponents η_{Tz} and η_{Ez} are shown as a function of particle stiffness in Fig. 9. Also shown is the exponent in the scaling relationship,

$$E_c \propto T^{\eta_{ET}}, \tag{9}$$

between the contact and the kinetic energies per particle, derived from plots of the contact energy versus kinetic energy

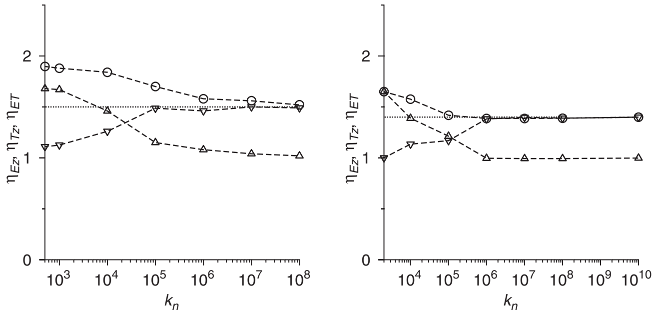

(a) (b)

FIG. 9. The exponent η_{Tz} in Eq. (8) (△), η_{Ez} in Eq. (8) (○), and the exponent η_{ET} in Eq. (9) (▽). The predicted exponent η_{TE}, from the scaling relationship between the kinetic and contact energies, $\eta_{ET} = 1.5$ for the linear contact model and $\eta_{ET} = 1.4$ for the Hertzian contact model, is shown by the dotted lines.

similar to Fig. 4, which are not shown here for conciseness. The kinetic energy per particle increases linearly with depth when the particle stiffness is greater than 10^4 for the linear contact model and 10^5 for the Hertzian contact model. The scaling exponent for the contact energy with height η_{Ez} is close to 1.5 for particle $k_n > 10^4$ for the linear contact model and $k_n > 10^5$ for the Hertzian contact model, and it shows a modest increase as the particle stiffness is decreased. The exponent η_{ET} [Eq. (9)] is about 1.5 for the linear contact model for $k_n > 10^4$ and about 1.4 for the Hertzian contact model for $k_n > 10^5$.

A scaling relationship between the kinetic and contact energies per particle can be derived in the collisional regime. The time-averaged ratio of the contact energy and kinetic energy per particle scales as the ratio of the maximum contact and kinetic energies times the period of a collision divided by the time between collisions. When particles interact through discrete collisions, the maximum contact energy during a contact is comparable to the maximum kinetic energy between collisions, both scaling proportional to T. The period of a collision τ_c depends on the type of contact model used. For the linear model, the period of a collision is independent of the maximum displacement and is proportional to $(m/k_n)^{1/2}$, where k_n is the normal particle stiffness and m is the particle mass. The average time between collisions scales as $T^{-1/2}$. Therefore, the ratio of contact and kinetic energies is expected to scale as $(m/k_n)^{1/2}T^{1/2}$. For the Hertzian model, the average period of a collision does depend on the average overlap between the particles, $\tau_c \sim (m/k_n\delta^{1/2})^{1/2}$. Since the maximum contact energy $\sim k_n\delta^{5/2}$ in a collision is comparable to the kinetic energy T between collisions, the characteristic overlap scales as $\delta \sim (T/k_n)^{2/5}$, and the period of a collision is $\tau_c \sim (m^{1/2}k_n^{-2/5}T^{-1/10})$. The time between collisions is proportional to $T^{-1/2}$. Therefore, the ratio of the contact energy and kinetic energy per particle scales as $(m^{1/2}T^{2/5}/k_n^{2/5})$.

The results for η_{ET} in Fig. 9 are consistent with those predicted by the above scaling arguments shown by the dotted lines, above the rheological threshold. Figure 9(a) shows that the exponent η_{ET} in Eq. (9) is close to 1.5 for high particle stiffness $k_n > 10^4$ for the linear contact model, consistent with the above reasoning that the ratio of the contact and kinetic energies is proportional to $T^{1/2}$. Similarly, for the Hertzian contact model, Fig. 9 shows that η_{ET} is close to 1.4 for $k_n > 10^5$, consistent with the above scaling analysis that the ratio of the contact and kinetic energies is proportional to $T^{2/5}$. Below the rheological threshold, the exponent η_{ET} systematically decreases as the particle stiffness is decreased, and approaches a value close to 1 for the lowest particle stiffness considered here.

The scaling of the height-averaged contact and kinetic energies per particle and the energy ratio is shown as a function of the particle stiffness in Fig. 10. The kinetic energy per particle decreases by about one order of magnitude for the range of particle stiffnesses considered here, and approaches a constant value in the limit of high particle stiffness for both the linear and the Hertzian models. In contrast, the contact energy per particle exhibits a monotonic decrease as the particle stiffness is increased. The ratio of the kinetic and contact energies per particle shows the scaling $k_n^{-1/2}$ for the linear contact model and $k_n^{-2/5}$ for the Hertzian contact model when the particle stiffness exceeds the rheological threshold, as expected in the collisional regime.

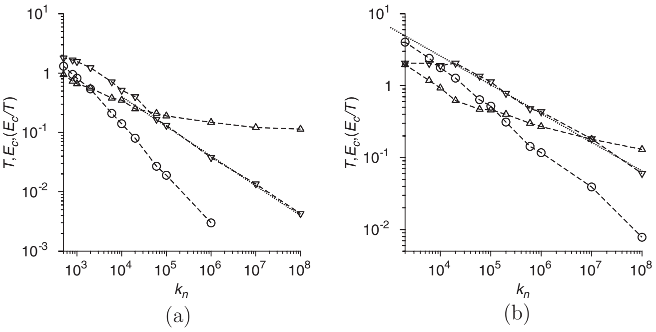

(a) (b)

FIG. 10. The height-averaged kinetic energy per particle (○), contact energy per particle (△), and the ratio of the contact and kinetic energies ▽ a function of the particle stiffness for the linear contact model (a) and the Hertzian contact model (b). The dotted line has a slope $-1/2$ in panel (a) and $-2/5$ in panel (b).

V. FORCE AND ENERGY DISTRIBUTIONS

The distribution of the magnitude of the contact force between pairs of particles, $F = |\mathbf{F}_{ij}|$, and the energy of the contacts between pairs of particles, E_c, are considered. Since the magnitudes of the contact force and energy change as the height changes, the distribution functions are plotted for $(F/\bar{F})$ and $(E_c/\bar{E}_c)$ at a fixed height. Height intervals in the z direction of thickness 4 particle diameters are used for determining the average values $\bar{F}$ and $\bar{E}_c$, and the probability distribution functions $P(F/\bar{F})$ and $P(E_c/\bar{E}_c)$ are determined as a function of height.

A striking feature of the force and contact energy distributions is the invariance with height. The form of the distribution function is found to be independent of height, even though the average values of the contact forces and energies do vary significantly with height. In Fig. 11, the distribution functions for the magnitudes of the contact forces are shown at four different heights, ranging from 6 particle diameters from the base to 62 particle diameters from the base. There is virtually no difference, to within the simulation resolution, in the distribution function for the force when the height changes from 6 to 62 particle diameters. This is despite the variation of a factor of 10 in the magnitude of the force when the height changes from 6 to 62 particle diameters, as shown in Fig. 6. The variation of the contact energy distribution function with height, shown in Fig. 12, also shows almost no variation when the height is varied between 6 and 62 particle diameters from the base, despite a variation of a factor of 10 in the value of the contact energy, as shown in Fig. 8. This feature is observed for the statistics of the normal and tangential forces at contact, as well as the tangential and normal components of the contact energies. Thus, there seems to be a universality in the form of the distribution of forces and contact energies, and an invariance with height, for both the linear and the Hertzian contact model. However, it is also clear from Fig. 11 that the force distributions do depend on the contact model. The force distribution has a maximum at the origin for the Hertzian contact model, whereas the maximum is at a finite value of the

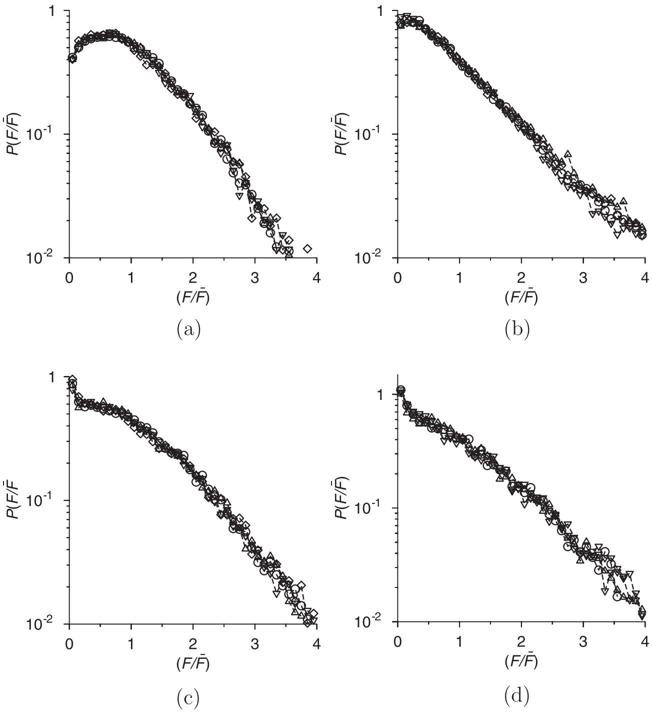

(a) (b)

(c) (d)

FIG. 11. The distribution function for the contact force magnitude at a height of 6 particle diameters from the base (○), 26 particle diameters from the base (△), 46 particle diameters from the base (▽), and 62 particle diameters from the base (◇) for the linear contact model with particle stiffness $k_n = 10^3$ (a) and 10^8 (b), and for the Hertzian particle contact model for particle stiffness 10^4 (c) and 10^8 (d).

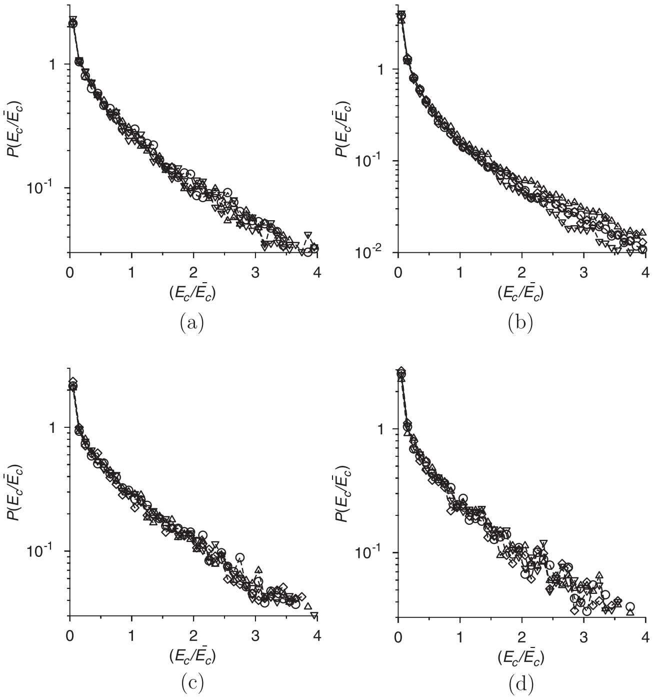

(a) (b)

(c) (d)

FIG. 12. The distribution function for the contact energy at a height of 6 particle diameters from the base (○), 26 particle diameters from the base (△), 46 particle diameters from the base (▽), and 62 particle diameters from the base (◇) for the linear contact model with particle stiffness $k_n = 10^3$ (a) and 10^8 (b), and for the Hertzian particle contact model for particle stiffness 10^4 (c) and 10^8 (d).

force for the linear contact model. Though the contact energy distributions appear more uniform in Fig. 12, there are subtle differences in the form of the contact energy distribution, which are discussed next.

Since the distributions are invariant with height, we use height-averaged distributions in order to examine the effect of particle stiffness on the force and energy distributions. In the following analysis, the particle distribution functions are averaged over the bulk of the flow excluding regions of height 5 particle diameters at the bottom and at the top.

The height-averaged force and contact energy distributions are shown as a function of the particle stiffness for the linear contact model in Fig. 13, and the Hertzian contact model in Fig. 14. In contrast to Figs. 11 and 12, the distributions in Figs. 13 and 14 are specifically shown on log-log graphs to highlight the differences in the distribution functions for small force/energy values. For the linear contact model, there is a maximum in the force distribution at a nonzero value of the force, as shown in Fig. 13. In addition, a clear transition in the form of the distribution function is observed as the particle stiffness is decreased for the linear contact model. There is very little variation in the force distribution when the particle stiffness is increased from 5×10^2 to 10^6, and when it is increased from 10^7 to 10^8. However, there is a significant change in the force distribution when the stiffness is increased from 10^6 to 10^7. The same features are observed in the contact energy distribution shown in Fig. 13. The contact energy distribution shows two distinct forms, one for $k_n \leqslant 10^6$ and the second for $k_n \geqslant 10^7$. There is a distinct shift in the form of the contact energy distribution when the particle stiffness increases from 10^6 to 10^7.

For $k_n \geqslant 10^7$, the contact force distribution is very well fitted by an exponential distribution, $P(F/\bar{F}) = \exp(-F/\bar{F})$, shown by the dotted line in Fig. 13(a). This is also evident in the comparison on a linear-log scale in Fig. 11(b). However,

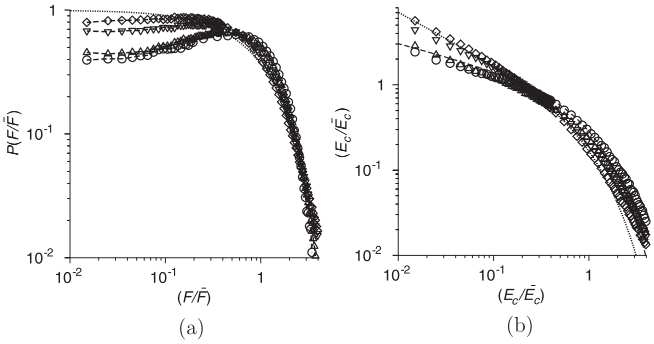

(a) (b)

FIG. 13. The height-averaged distribution function for the force magnitude (a) and the contact energy (b) for the linear contact model for particle stiffness $k_n = 5\times10^2$ (○), $k_n = 10^6$ (△), $k_n = 10^7$ (▽), and $k_n = 10^8$ (◇). In panel (a), the dotted line is the exponential distribution. In panel (b), the dashed line is the Gamma distribution $P_\Gamma(0.7,(E_c/\bar{E}_c))$, and the dotted line is the Gamma distribution $P_\Gamma(0.4,(E_c/\bar{E}_c))$.

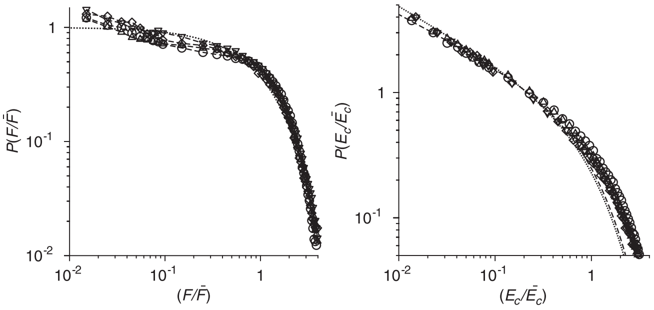

(a) (b)

FIG. 14. The height-averaged distribution function for the force magnitude (a) and the contact energy (b) for the Hertzian contact model for particle stiffness $k_n = 2\times10^3$ (○), $k_n = 10^7$ (△), $k_n = 10^8$ (▽), and $k_n = 10^{10}$ (◇). In panel (a), the dotted line is the exponential distribution. In panel (b), the dashed line is the Gamma distribution $P_\Gamma(0.6,(E_c/\bar{E}_c))$, and the dotted line is the Gamma distribution $P_\Gamma(0.55,(E_c/\bar{E}_c))$.

for $k_n \leqslant 10^6$, the distribution function is significantly different from an exponential distribution, and it has a clear maximum at a finite value of the force magnitude. The contact energy distribution, interestingly, exhibits a power-law divergence for low values of the contact energy. Two distinct power laws, one for $k_n \leqslant 10^6$ and a second faster-diverging power law for $k_n \geqslant 10^7$, are clearly discernible in Fig. 13(b). The dashed and dotted lines in Fig. 13(b) show fits to Gamma distributions,

$$P_\Gamma(a,x) = \frac{x^{(a-1)}\exp(-x)}{\Gamma(a)}. \tag{10}$$

The Gamma distribution $P_\Gamma(0.7,(E_c/\bar{E}_c))$ provides a good fit for the energy distribution function for $k_n \leqslant 10^6$, while the Gamma distribution with a lower exponent $P_\Gamma(0.4,(E_c/\bar{E}_c))$ fits the data for $k_n \geqslant 10^7$. It should be noted that there is a departure from the Gamma distribution for higher values of $(E_c/\bar{E}_c)$ greater than about 2: the high-energy tail in the actual distribution function is larger than that in the Gamma distribution. However, for lower values of the contact energy, the distribution function is well represented by the Gamma distribution.

A transition in the form of the contact energy distribution with particle stiffness is also observed for the Hertzian contact model, shown in Fig. 14(b). There appears to be a divergence for low force in the force distribution shown in Fig. 14(a), but the magnitude of the power-law exponent is too low to be inferred from the data. Though the force distribution does appear to have the same form independent of particle stiffness, there is a hint of a transition when the particle stiffness is increased from 10^7 to 10^8. There is very little change in the form of the force distribution for $2\times10^3 \leqslant k_n \leqslant 10^7$, and for $10^8 \leqslant k_n \leqslant 10^{10}$. The contact energy distribution in Fig. 14(b) clearly exhibits a power-law divergence for low contact energy. There is a small but discernible change in the power-law exponent when the particle stiffness is increased from 10^7 to 10^8; there is very little change in the exponent for $k_n \leqslant 10^7$ or for $k_n \geqslant 10^8$. The data for $k_n \leqslant 10^7$ are well fitted by the Gamma distribution $P_\Gamma(0.6,(E_c/\bar{E}_c))$, while those for $k_n \geqslant 10^8$ are fitted by a Gamma distribution $P_\Gamma(0.55,(E_c/\bar{E}_c))$. There is only a small change in the power-law exponent, with the former diverging proportional to $(E_c/\bar{E}_c)^{-0.4}$ while the latter diverges as $(E_c/\bar{E}_c)^{-0.45}$. However, even this small difference is visible in the fits for the distribution in Fig. 14(b).

The transition in the form of the distribution function corresponds to the transition in the contact regime from the binary to the multibody contact regime. Figure 5(a) shows that the coordination number crosses 1 when the particle stiffness is decreased from 10^7 to 10^6 for the linear contact model; the transition in the form of the distribution functions for the linear contact model is observed precisely in this range in Fig. 13. Similarly, Fig. 5(b) shows that the coordination number exceeds 1 when the particle stiffness is decreased from 10^8 to 10^7 for the Hertzian contact model, and the transition in the form of the distribution function is observed in this range in Fig. 14. Thus, the change in the form of the distribution function appears to be correlated to the change in the flow dynamics from a binary contact regime to a multibody contact regime as the particle stiffness is decreased.

VI. TRANSITION

The transition from a disordered to an ordered flow is an intriguing phenomenon observed in the granular flow down an inclined plane due to the decrease in the base roughness. The transition appears to be a universal phenomenon which is observed for different types of bases, including frozen-particle bases consisting of frozen particles with random and hexagonally ordered arrangements, or sinusoidal bases with modulation in the streamwise and spanwise directions [40]. The base roughness is defined as the ratio of the base and flowing particle diameters for frozen-particle bases, and as the ratio of the amplitude of the base modulation and the flowing particle diameter for sinusoidal bases. There is a change in flow regime from a random to an ordered flow when the base roughness decreases by less than 1%; in the case of frozen-particle bases, this transition takes place when the roughness decreases from 0.57 to 0.56 for a random frozen-particle base, and from 1.35 to 1.34 for an ordered frozen-particle base. In the case of sinusoidal bases, the transition roughness depends on the wavelength of the sinusoidal modulation. The results for transition due to base roughness have been explained extensively earlier [37,39,40], and we provide a brief summary of those results here to introduce the indicators used to infer transition.

For both random and ordered flows, the flow properties in the bulk are independent of the type of base roughness and the base amplitude. However, there is a discontinuous change in the flow properties when there is a transition from a random to an ordered flow. These properties are shown for an ordered frozen-particle base in Fig. 15. The ordered flow consists of layers of particles parallel to the base sliding over each other, as shown by the number density profiles in Fig. 15(a). The number density is determined by counting the number of particles with centers within a differential volume, and dividing by the volume. The number density is independent of height when the particles are uniformly distributed, but show sharp maxima and minima when there is layering. The number density profiles in Fig. 15(a) show that there is the abrupt onset of layering when the base roughness is decreased from 1.35 to 1.34. There is

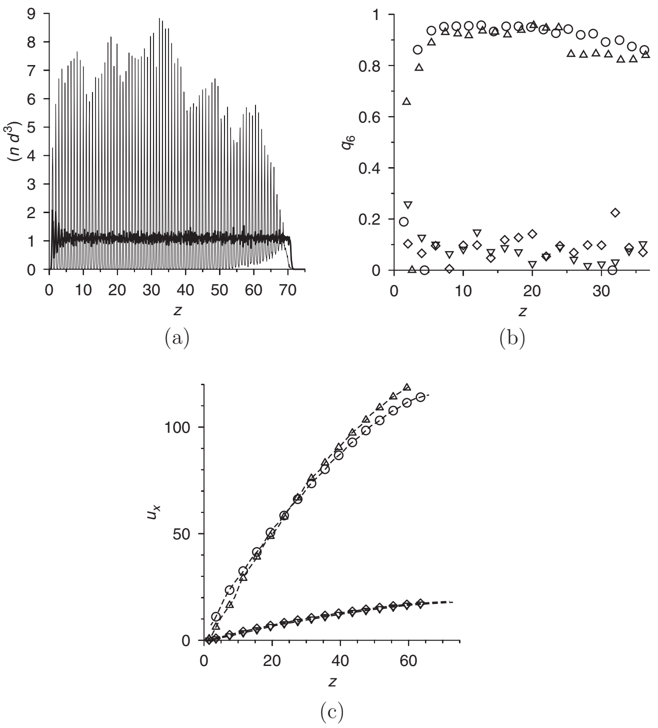

(a) (b)

(c)

FIG. 15. The variation with height of the number density (a), the q_6 order parameter (b), and the mean velocity (c) for the linear model with dimensionless particle stiffness $k_n = 10^7$, and for a hexagonally ordered frozen-particle base with base particle diameter 0.5 [○ in (b) and (c)], 1.34 [thin line in (a), △ in (b) and (c)], 1.35 [thick line in (a), ▽ in (b) and (c)], and 2.00 [◇ in (b) and (c)].

virtually no change in the number density profiles in the layered state when the base roughness is decreased below 1.34, and there is virtually no change in number density profiles in the random state when the base roughness is increased above 1.35. Within the layers, there is in-plane ordering, which is quantified by the in-plane hexagonal order parameter q_6 [37,39,40], which is close to 0 in the random state and is 1 when there is hexagonal ordering. The transition from random to a hexagonally ordered layers is observed when the base particle diameter is decreased from 1.35 to 1.34 for a hexagonally ordered base, as shown in Fig. 15(b). There is also a dramatic difference in the mean velocity profiles for the random and ordered states, as shown in Fig. 15(c). The mean velocity profiles are well described by Bagnold profiles for both ordered and disordered flows, but for equal angle of inclination and particle properties, the mean velocity in the ordered flow is about 10 times larger than that in the random flow.

Here, we examine the effect of a change in the particle stiffness on the order-disorder transition. Simulations are carried out for a flat base, which is the limit of zero base roughness for all the different base topologies. The flow structure is examined as the stiffness of the interparticle contacts is decreased systematically for the flow over a flat base. The results are shown in Fig. 16. It is observed that for both the linear and Hertzian contact models, the flow is ordered for high particle stiffness. As the stiffness is decreased, the transition disappears when the dimensionless particle stiffness is decreased from 6×10^4 to 2×10^4 for the linear model, and from 6×10^5 to 2×10^5 for the Hertzian contact model. This is shown by the disappearance of the maxima in the number density profiles in Figs. 16(a) and 16(b), and the decrease in the q_6 order parameter in Figs. 16(c) and 16(d) from the value close to 1 for hexagonal close packing, to a small value when the particle stiffness decreases below the critical value. This indicates a transition from an ordered to a random state as the particle stiffness is decreased. This is also confirmed by the mean velocity profiles in Figs. 16(e) and 16(f), which decreases by a factor of 10 at the transition from the ordered to the disordered states.

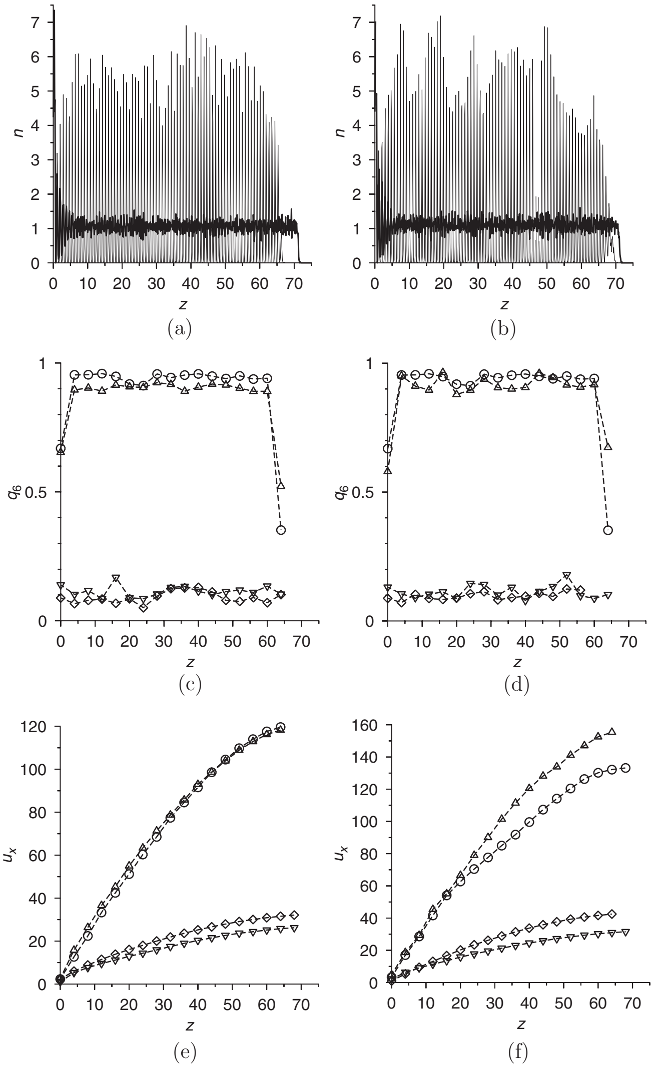

(a) (b)

(c) (d)

(e) (f)

FIG. 16. The variation with height of the number density [(a) and (b)], the q_6 order parameter [(c) and (d)], and the mean velocity [(e) and (f)] for the linear model [(a), (c), and (e)] and the Hertzian model [(b), (d), and (f)]. In panels (a), (c), and (e) particle stiffness $k_n = 10^7$ [○ in (c) and (e)], $k_n = 6\times10^4$ [thin line in (a), △ in (c) and (e)], $k_n = 2\times10^4$ [thick line in (a), ▽ in (c) and (e)], and 5×10^2 [◇ in (c) and (e)]. In panels (b), (d), and (f) particle stiffness $k_n = 10^8$ [○ in (d) and (f)], $k_n = 6\times10^5$ [thin line in (b), △ in (d) and (f)], $k_n = 2\times10^5$ [thick line in (b), ▽ in (d) and (f)], and 2×10^3 [◇ in (d) and (f)].

Simulations have been carried out for all types of bases, including frozen-particle and sinusoidal bases, and it has been observed that the transition occurs for the same particle stiffness shown in Fig. 16. When the particle stiffness is greater than 6×10^4 for the linear model, a transition from a random to an ordered state is observed when the base roughness is decreased. When the particle stiffness is less then 2×10^4 for the linear model, there is no transition and the flow is in the random state independent of base roughness. For the Hertzian model, there is transition when the particle stiffness is greater than 6×10^5 when the base roughness is decreased, and the flow over a flat base is found to be ordered. There is no transition when the particle stiffness is decreased below 2×10^5, and the flow is always disordered.

Thus, the transition phenomenon appears to be a characteristic of hard-particle systems, and transition disappears when the particle stiffness decreases below a threshold. This threshold corresponds to the rheological threshold for progression from Bagnold to non-Bagnold rheology, reported in the stress-strain rate (Fig. 3) and temperature-strain rate (Fig. 4) graphs, and the progression of the scaling exponents in Fig. 5. This threshold is different from the threshold for the transition from the binary to multibody contact regime reported in the force and energy distributions in Figs. 13 and 14.

VII. CONCLUSIONS

A. Volume fraction and coordination number

It is already well known, since the simulations of Silbert *et al.* [4], that there is a lack of a one-to-one relationship between the granular temperature and the volume fraction in dense granular flows. Though the granular temperature increases approximately linearly from top to bottom, the volume fraction is a constant. This is because the increase in overburden with depth is balanced by an increase in the agitation of the particles, instead of an increase in the volume fraction. In the present system with multibody contacts, it is found that there is an increase in the coordination number and an approximately linear increase in the average force per particle with depth in order to balance the overburden, though the volume fraction is a constant. It should be noted that the constant volume fraction condition emerges from the invariance of the ratio of the shear and normal stresses with height. If the Bagnold coefficients are monotonic functions of volume fraction, it follows that the volume fraction is invariant with height. However, there is no such restriction on either the temperature, collision frequency, or coordination number. This results in the unusual feature of dense granular flows down an inclined plane that there is a variation in the granular temperature and coordination number with height even though the volume fraction is a constant for sufficiently high particle stiffness.

The more surprising result here is the increase in the coordination number as the particle stiffness is decreased. Even though the coordination number increases from about 0.5 to about 2 when the particle stiffness is decreased from 10^8 to 10^4 for the linear contact model, and there is some change in the mean velocity and granular temperature profiles, there is no perceptible change in the volume fraction. This implies that the volume-fraction dependence of the ratio of the Bagnold coefficients shows no variation with particle stiffness, though the individual coefficients do vary, and the coordination number exhibits a relatively large variation. Further work is required to better understand this behavior.

B. Rheology

There are two distinct rheological regimes depending on the particle stiffness. When the stiffness is greater than a "rheology threshold," which is between 2×10^4 and 6×10^4 for the linear contact model and between 2×10^5 and 6×10^5 for the Hertzian contact model, the Bagnold rheology is found to be valid, and all components of the stress are found to be proportional to the square of the strain rate, $(du_x/dz)^2$. The granular temperature is also proportional to $(du_x/dz)^2$. When the particle stiffness is reduced below this threshold, the rheology is similar to that of a power-law fluid with decreasing power-law exponent; the exponent in the stress-strain rate relationship decreases to about 1 and that in the granular temperature-strain rate relationship decreases to about 1.5 for the lowest values of particle stiffness that could be accessed here. Though this appears to be similar to that for a Newtonian fluid, where the stress is proportional to (du_x/dz), it should be noted that all components of the stress are found to be proportional to the strain rate; in contrast, in Newtonian fluids, only the symmetric traceless part of the stress is proportional to the strain rate, while the pressure is fixed by the incompressibility condition.

The progression from Bagnold to non-Bagnold rheology occurs when the coordination number is between 1.5 and 2 for both the linear and the Hertzian contact models. Clearly, the Bagnold rheology is valid even when the particles are in the multibody contact regime, and the coordination number is not a good indicator of the rheology. Similarly, we also find that the measures such as the magnitude of the resultant force and total force on a particle do not show any indication of the progression from Bagnold to non-Bagnold rheology. The indicator that correlates best to the change in rheology is the magnitude of the contact energy per particle and the kinetic energy per particle. The contact energy per particle decreases by 4–5 orders of magnitude as the particle stiffness is increased by 8 orders of magnitude, whereas the granular temperature shows a very modest decrease of less than 1 order of magnitude. In the Bagnold regime, the contact energy per particle is found to be smaller than the kinetic energy per particle, even though the coordination number is greater than 1. As the particle stiffness is decreased, the rheology progresses to the non-Bagnold regime when the contact energy per particle is comparable to the kinetic energy per particle. Thus, the ratio of the contact and kinetic energies is a better indicator of the rheology than the coordination number.

Another reliable indicator is the scaling of the contact and kinetic energies per particle with height and with particle stiffness. In the binary contact regime, we have derived scalings of the ratio of the contact and kinetic energies per particle. These scalings correlate best with the progression in the rheology as the particle stiffness is decreased. When the particle stiffness is above the rheological threshold, the scalings for the ratio of contact and kinetic energies are identical to those predicted by the binary collision approximation, even though the system is in the multibody contact regime. When the particle stiffness is below the rheological threshold, the scaling laws are not in agreement with the predictions for the binary collision regime. Thus, there is a strong correlation between the scaling of the energy ratio and the rheology.

The $\mu(I)$ rheology has been widely used to model the flow of dense granular materials [48–50], where the parameter μ (ratio of the shear stress and pressure) is expressed as a function of the inertia number I which is proportional to the strain rate scaled by the square root of the pressure. The $\mu(I)$ rheology follows naturally if the stresses satisfy Bagnold law. In Bagnold rheology, both the pressure and shear stress are proportional to $(du_x/dz)^2$ for the inclined plane flow. Therefore, the ratio $\mu = (\sigma_{xz}/p)$ can be written as function of $I = (d(du_x/dz)/\sqrt{p/\rho})$, and the function $\mu(I)$ depends only on the volume fraction in the hard-particle limit. Here, d is the particle diameter and ρ is the density. The present analysis establishes a lower threshold for the particle stiffness, below which the Bagnold law is not valid. When the particle stiffness is below this threshold, there is a power-law dependence of the pressure and stress on the strain rate with equal exponents. This would imply that the $\mu(I)$ rheology would also need to be modified for particle stiffness below the threshold, and the parameter I would need to be redefined by scaling the pressure with the appropriate power of the strain rate.

C. Force and energy distribution

The present study has revealed that the contact force and energy distributions are invariant with depth for fixed particle stiffness and angle of inclination, even though the magnitudes of the contact energy varies by more than 1 order of magnitude when the height is varied by 60 particle diameters. This invariance with height is observed for the distributions of all the dynamical contact properties such as the tangential and normal forces, the force magnitude, and the contact energy. The invariance of the distribution function suggests that the entire flow is in one single contact regime independent of height. If all the force distributions have an identical form independent of height, the particle weight is balanced by the variation in the average of the distribution.

The form of the contact force distribution is strongly dependent on the particle contact model. The peak of the force distribution is at zero force for the Hertzian contact model, but it is at a nonzero force for the linear contact model. The force distributions do have an exponential decay in the high-force limit, but the details of the distribution in the low-force limit do depend on the contact model. The difference in the form of the force distribution could be due to the following. For the Hertzian contact model, the restoring force scales as $\delta_n^{3/2}$, where δ_n is the normal displacement. Therefore, the restoring force for small δ_n is much smaller than that for the linear model, where the restoring force is proportional to δ_n. The contacts are much softer for small displacements, and due to this there is a maximum in the force distributions around zero force. In comparison, the contacts for the linear force model are stiffer for small displacements, and this results in a larger probability at finite force values.

The contact energy distributions for both the models are found to be well fitted by Gamma distributions with different shape parameters and different power-law divergences at zero energy. This universality in the contact energy distributions has not been reported before.

With decreasing particle stiffness, the change from the binary to the multibody contact regime is clearly reflected in the force and energy distributions. There is a distinct shift in the distribution function when the scaled particle stiffness is decreased from 10^7 to 10^6 for the linear contact model and 10^8 to 10^7 for the Hertzian contact model; in both cases, the coordination number is greater than 1 for the lower particle stiffness and less than 1 for the higher particle stiffness. The shift in the distribution is clearly visible for the linear contact model, and is discernible even for the Hertzian contact model. Further analysis is required in order to predict the forms of the force and contact energy distribution functions, especially the Gamma distributions for the contact energy distribution.

Thus, there are two distinct thresholds that are revealed by the present study. The contact regime threshold between the binary and multibody contact regime is characterized by the increase in the coordination number above 1. At this threshold, there is a distinct shift in the forms of the force and energy distributions. However, there is no shift in the rheology or the ratios of the kinetic and contact energies per particle.

There is a different rheological threshold between Bagnold and non-Bagnold rheology. At this threshold, the ratio of the contact and kinetic energy per particle passes through 1; the contact energy is larger (smaller) than the kinetic energy below (above) this threshold. A strong correlation is found between the rheology and the scalings for the ratio of the contact and kinetic energy per particle. This ratio follows the scalings applicable for the binary contact regime above the rheological threshold, but it deviates from these scalings below this threshold. The system is already in the multibody contact regime at the rheological threshold, though the scaling of the energy ratio is identical to that in the binary contact regime.

D. Transition

One of the most important results of the present analysis is that there is a “transition threshold” coinciding with the “rheological threshold” in the particle stiffness. Above this threshold, there is a discontinuous transition from a disordered flow to an ordered flow as the base roughness is decreased. Below this threshold, there is no transition, and the flow over even a flat base with no roughness is in the disordered state. Thus, transition is observed only for systems which follow Bagnold rheology, and is not observed for systems where the rheology is different. This confirms that the transition phenomenon is exhibited only by hard-particle systems, similar to the crystallization transition in a gas of elastic hard particles at equilibrium.

ACKNOWLEDGMENTS

The authors thank the J. R. D. Tata Trust and the Department of Science and Technology, Government of India, for financial support.

[1] R. Bagnold, Experiments on a gravity-free dispersion of large solid spheres in a Newtonian fluid under shear, Proc. R. Soc. London A **225**, 49 (1954).

[2] R. Bagnold, The flow of cohesionless grains in fluids, Proc. R. Soc. London A **249**, 235 (1954).

[3] M. L. Hunt, R. Zenit, C. S. Campbell, and C. E. Brennen, Revisiting the 1954 suspension experiments of R. A. Bagnold, J. Fluid Mech. **452**, 1 (2002).

[4] L. E. Silbert, D. Ertas, G. S. Grest, T. C. Halsey, D. Levine, and S. J. Plimpton, Granular flow down an inclined plane: Bagnold scaling and rheology, Phys. Rev. E **64**, 051302 (2001).

[5] K. A. Reddy and V. Kumaran, Applicability of constitutive relations from kinetic theory for dense granular flows, Phys. Rev. E **76**, 061305 (2007).

[6] K. A. Reddy and V. Kumaran, Dense granular flow down an inclined plane: A comparison between the hard particle model and soft particle simulations, Phys. Fluids **22**, 113302 (2010).

[7] V. Kumaran, Dense granular flow down an inclined plane: From kinetic theory to granular dynamics, J. Fluid Mech. **599**, 121 (2008).

[8] C. S. Campbell, Stress-controlled elastic granular shear flows, J. Fluid Mech. **539**, 273 (2005).

[9] C. Campbell, Clusters in dense-inertial granular flows, J. Fluid Mech. **687**, 341 (2011).

[10] R. Brewster, L. E. Silbert, G. S. Grest, and A. J. Levine, Relationship between interparticle contact lifetimes and rheology in gravity-driven granular flows, Phys. Rev. E **77**, 061302 (2008).

[11] D. M. Mueth, H. M. Jaeger, and S. R. Nagel, Force distribution in a granular medium, Phys. Rev. E **57**, 3164 (1998).

[12] T. S. Majumdar and R. P. Behringer, Contact force measurements and stress-induced anisotropy in granular materials, Nature (London) **435**, 1079 (2005).

[13] R. R. Hartley and R. P. Behringer, Logarithmic rate dependence of force network in sheared granular materials, Nature (London) **421**, 928 (2003).

[14] R. Blumenfeld and S. F. Edeards, Granular Entropy: Explicit Calculations for Planar Assemblies, Phys. Rev. Lett. **90**, 114303 (2003).

[15] S. Henkes, C. O'Hern, and B. Charaborty, Entropy and Temperature of a Static Granular Assembly: An *Ab Initio* Approach, Phys. Rev. Lett. **99**, 038002 (2007).

[16] S. N. Coppersmith, C.-h. Liu, S. Majumdar, O. Narayan, and T. A. Witten, Model for force fluctuations in bead packs, Phys. Rev. E **53**, 4673 (1996).

[17] J. Javier Brey, M. J. Ruiz-Montero, and F. Moreno, Hydrodynamics of an open vibrated granular system, Phys. Rev. E **63**, 061305 (2001).

[18] V. Kumaran, Temperature of a granular material "fluidized" by external vibrations, Phys. Rev. E **57**, 5660 (1998).

[19] V. Kumaran, Kinetic theory for a vibro fluidised bed, J. Fluid Mech. **364**, 163 (1998).

[20] P. K. Haff, Grain flow as a fluid-mechanical phenomenon, J. Fluid Mech. **134**, 401 (1983).

[21] C. K. K. Lun, S. B. Savage, D. J. Jeffrey, and N. Chepurniy, Kinetic theories for granular flow: Inelastic particles in Couette flow and slightly inelastic particles in a general flowfield, J. Fluid Mech. **140**, 223 (1984).

[22] C. K. K. Lun, Kinetic theory for the flow of dense, slightly inelastic, slightly rough spheres, J. Fluid Mech. **233**, 539 (1991).

[23] J. T. Jenkins and M. W. Richman, Grad's 13-moment system for a dense gas of inelastic spheres, Arch. Ration. Mech. Anal. **87**, 355 (1985).

[24] J. T. Jenkins, Dense shearing flows of inelastic disks, Phys. Fluids **18**, 103307 (2006).

[25] J. T. Jenkins, Dense inclined flows of inelastic spheres, Granular Matter **10**, 47 (2007).

[26] N. Sela, I. Goldhirsch, and S. H. Noskowicz, Kinetic theoretical study of a simply sheared two dimensional granular gas to Burnett order, Phys. Fluids **8**, 2337 (1996).

[27] N. Sela and I. Goldhirsch, Hydrodynamic equations for rapid flows of smooth inelastic spheres, to Burnett order, J. Fluid Mech. **361**, 41 (1998).

[28] I. Goldhirsch and N. Sela, Origin of normal stress differences in rapid granular flows, Phys. Rev. E **54**, 4458 (1996).

[29] V. Kumaran, Constitutive relations and linear stability of a sheared granular flow, J. Fluid Mech. **506**, 1 (2004).

[30] V. Kumaran, The constitutive relation for the granular flow of rough particles, and its application to the flow down an inclined plane, J. Fluid Mech. **561**, 1 (2006).

[31] A. V. Orpe, V. Kumaran, K. A. Reddy, and A. Kudrolli, Fast decay of the velocity autocorrelation function in dense shear flow of inelastic hard spheres, Europhys. Lett. **84**, 64003 (2008).

[32] V. Kumaran, Dynamics of a dilute sheared inelastic fluid. I. Hydrodynamic modes and velocity correlation functions, Phys. Rev. E **79**, 011301 (2009).

[33] V. Kumaran, Dynamics of a dilute sheared inelastic fluid. II. The effect of correlations, Phys. Rev. E **79**, 011302 (2009).

[34] D. Berzi and J. T. Jenkins, Steady shearing flows of deformable inelastic spheres, Soft Matter **11**, 4799 (2015).

[35] S. Chialvo, J. Sun, and S. Sundaresan, Bridging the rheology of granular flows in three regimes, Phys. Rev. E **85**, 021305 (2012).

[36] M. Otsuki and H. Hayakawa, Critical scaling near jamming transition for frictional granular particles, Phys. Rev. E **83**, 051301 (2011).

[37] V. Kumaran and S. Maheshwari, Transition due to base roughness in the dense granular flow down an inclined plane, Phys. Fluids **24**, 053302 (2012).

[38] S. Maheshwari and V. Kumaran, The effect of base dissipation on the granular flow down an inclined plane, Granular Matter **14**, 209 (2012).

[39] V. Kumaran and S. Bharathraj, The effect of base roughness on the development of a dense granular flow down an inclined plane, Phys. Fluids **25**, 070604 (2013).

[40] S. Bharathraj and V. Kumaran, Effect of base topography on dynamics and transition in a dense granular flow, J. Fluid Mech. **832**, 600 (2017).

[41] B. J. Alder and T. E. Wainwright, Phase transition in elastic disks, Phys. Rev. **127**, 359 (1962).

[42] W. G. Hoover and F. H. Ree, Melting transition and communal entropy for hard spheres, J. Chem. Phys. **49**, 3609 (1968).

[43] V. S. Kumar and V. Kumaran, Voronoi cell volume distribution and configurational entropy of hard spheres, J. Chem. Phys. **123**, 114501 (2005).

[44] V. S. Kumar and V. Kumaran, Voronoi neighbor statistics of homogeneously sheared inelastic hard disks and hard spheres, Phys. Rev. E **73**, 051305 (2006).

[45] V. S. Kumar and V. Kumaran, Bond-orientational analysis of hard-disk and hard-sphere structures, J. Chem. Phys. **124**, 204508 (2006).

[46] M. H. Cohen and G. S. Grest, Liquid-glass transition, a free-volume approach, Phys. Rev. B **20**, 1077 (1979).

[47] P. A. Cundall and O. D. L. Strack, A discrete numerical model for granular assemblies, Geotechnique **29**, 47 (1979).

[48] G. D. R. MiDi, On dense granular flows, Eur. Phys. J. E **14**, 341 (2004).

[49] P. Jop, Y. Forterre, and O. Pouliquen, A constitutive law for dense granular flows, Nature (London) **441**, 727 (2006).

[50] P. Jop, Rheological properties of dense granular flows, C. R. Phys. **16**, 62 (2015).